J. Fluid Mech. (2013), *vol.* 730, *pp.* 193–219.
doi:10.1017/jfm.2013.300

Laminarization mechanisms and extreme-amplitude states in rapidly rotating plane channel flow

Stefan Wallin[1,2],†, **Olof Grundestam**[1,2] **and Arne V. Johansson**[2]

[1]Information and Aeronautical Systems, Swedish Defence Research Agency (FOI), SE-164 90 Stockholm, Sweden

[2]Linné Flow Centre, KTH Mechanics, SE-100 44 Stockholm, Sweden

(Received 12 January 2011; revised 3 June 2013; accepted 7 June 2013; first published online 30 July 2013)

Fully developed plane channel flow rotating in the spanwise direction has been studied analytically and numerically. Linear stability analysis reveals that all cross-flow modes are stable for supercritical rotation numbers, $Ro > Ro_c$, where Ro_c will approach 3 from below for increasing Reynolds number. Plane Tollmien–Schlichting (TS) waves are independent of rotation and always linearly unstable for supercritical Reynolds numbers. Direct numerical simulation (DNS) of the laminarization process reveals that the turbulence is damped when Ro approaches Ro_c. Hence, the laminarization is dominated by linear mechanisms. The flow becomes periodic for supercritical Reynolds numbers and rotation rates, i.e. when $Ro > Ro_c$ and $Re > Re_c$. At such rotation rates, all oblique (cross-flow) modes are damped and when the disturbance amplitude becomes small enough, the TS modes start to grow exponentially. Secondary instabilities are initially blocked by the rotation since all cross-flow modes are linearly stable and the breakdown to turbulence will be strongly delayed. Hence, the TS waves will reach extremely high amplitudes, much higher than for typical turbulent fluctuations. Eventually, the extreme-amplitude state with TS-like waves will break down to turbulence and the flow will laminarize due to the influence of the rapid rotation, thus completing the cycle that will then be repeated. This flow is strongly dominated by linear mechanisms, which is remarkable considering the extremely high amplitudes involved in the processes of laminarization of the turbulence at $Ro \geqslant Ro_c$ and the growth of the unstable TS waves.

Key words: instability, rotating turbulence, transition to turbulence

1. Introduction

Turbulent flow is in general strongly influenced by system rotation as well as local rotation originating from e.g. streamline curvature. This occurs in swirling or recirculating flows for example, when the principal directions of the flow (e.g. the eigenvectors of the strain rate tensor) are rotating when following a mean streamline. This is of practical importance in engineering flows like rotor-machinery flows, flow over curved surfaces and in curved or rotating pipes and channels as well as in

† Email address for correspondence: stefan.wallin@foi.se

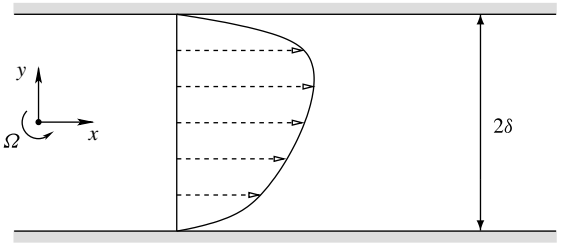

FIGURE 1. Geometry and mean flow of turbulent channel flow.

swirling flows, appearing in a wide variety of applications. Also, in geophysical flows the influence of rotation is of great importance.

Fully developed turbulent plane channel flow rotating in the spanwise direction has often been used for illustrating rotational effects on turbulent flow. The flow is destabilized by the Coriolis force on the pressure side and stabilized on the opposite side, the suction side. Moreover, this flow has many similarities with turbulent flow over curved surfaces and turbulent shear flows with buoyancy effects. The flow is illustrated in figure 1. The Coriolis force pushes the flow towards the lower side of the channel at $y = -\delta$ which is called the pressure side. Experimental studies by Johnston, Halleen & Lezius (1972) and Nakabashi & Kitoh (1996) as well as numerical studies by Kristoffersen & Andersson (1993) and Lamballais, Lesieur & Métais (1996) have established that for moderate rotation rates the turbulence is strongly enhanced on the pressure side and is damped or even laminarized on the suction side. Numerical simulations by Wu & Kasagi (2004) with a rotation vector combining all three unit directions revealed other interesting aspects of rotating flows. However, the spanwise component of the rotation vector dominates over the other components in terms of the influence on the flow.

The differences in turbulence level between the two sides result in an asymmetric mean velocity profile that has a core-region slope close to twice the system rotation rate ($\partial U/\partial y = 2\Omega$). This means that the mean-flow absolute vorticity, defined as the vorticity measured in the inertial non-rotating frame, will vanish in this region. In the present study, the Reynolds and rotation numbers are defined as

$$Re \equiv \frac{U_b \delta}{\nu}, \quad Ro \equiv \frac{2\Omega\delta}{U_b}, \tag{1.1}$$

where δ is the channel half-height, U_b is the bulk (or mean) velocity, Ω is the channel spanwise rotation rate and ν is the kinematic viscosity of the fluid.

Non-rotating plane Poiseuille flow is linearly stable up to a critical Reynolds number where the so-called Tollmien–Schlichting waves become unstable. The critical Reynolds number was derived by Lakin, Ng & Reid (1978) as $Re_c = 3846.5$ and by Orszag (1971) as $Re_c = 3848.15$ using accurate numerical solutions of the Orr–Sommerfeld equations, which is slightly higher than the earlier value $Re_c = 3570$ derived by Lin (1955). In the original formulations the critical Reynolds number was based on the centreline velocity, which is 3/2 times the bulk velocity used in the present definition. Even a small amount of rotation will strongly enhance the flow instability and the critical transitional Reynolds number decreases down to $Re_c \approx 44$ for the rotation number $Ro = 0.5$. This was determined using numerical solutions of linear stability by Lezius & Johnston (1976) and also later by Alfredsson &

Persson (1989), who also verified the stability analysis results experimentally. The much lower critical Reynolds number associated with the Coriolis instability in the rotating case indicates that such a mechanism is much stronger than the corresponding Tollmien–Schlichting instabilities, also noted by Alfredsson & Persson (1989).

Streamwise roll cells have been observed by Alfredsson & Persson (1989) in moderately rotating flows for Reynolds numbers in good agreement with the linear theory. For increasing Reynolds number, secondary instabilities become visible before breakdown to turbulence. The formation of these secondary instabilities around nonlinear high-amplitude roll cells was analysed by Wall & Nagata (2006) and the resulting unstable structures were found to be in good agreement with observations in the experiments by Alfredsson & Persson (1989).

Roll-cell-like structures are also visible in fully turbulent flows observed experimentally by Johnston *et al.* (1972) and in numerical simulations by Kristoffersen & Andersson (1993) as well as by Grundestam, Wallin & Johansson (2008). However, Grundestam *et al.* did not observe steady roll cells, although roll-cell-like structures could be seen in snapshots of the flow field. These structures vanished in the time-averaged results. Coexistence of roll cells and turbulent secondary flow has also been observed in rotating Couette flow numerically by Bech & Andersson (1997) as well as experimentally by Tsukahara, Tillmark & Alfredsson (2010) in agreement with the analysis of Nagata (1998) of secondary instabilities around the nonlinear high-amplitude roll cells. Roll-cell-like modes are strongly linearly unstable in such flows and a significant amount of energy will be fed into such modes even after the flow has broken down to turbulence due to secondary and tertiary instabilities. Hence, these modes are also visible in fully developed turbulence. Similar coherent structures and turbulent secondary flow can coexist as well for flows not only with Coriolis forces, but also with buoyancy and Lorentz forces as shown from direct numerical simulations (DNS) by Brethouwer, Duguet & Schlatter (2012).

For higher rotation rates the flow will also start to laminarize on the pressure side and for $Ro = 3$ the roll cells are completely stabilized by the rotation, see Lezius & Johnston (1976). The stability parameter introduced by Bradshaw (1969), $B = 2Ro_l(2Ro_l - 1)$, can be used for assessing the possibility of inviscid instabilities. $Ro_l = \Omega/U'$ ($U' = \partial U/\partial y$) is here the local rotation number in the channel, also used by Grundestam *et al.* (2008), although Bradshaw analysed rotating homogeneous shear flow. For $B > 0$ the flow is rotationally stable, which is the case if the rotation number $Ro > 3$ for a parabolic velocity profile.

As pointed out by Grundestam *et al.* (2008) the linear stability analysis cannot predict whether turbulence would or could be sustained for $Ro > 3$ or if fully developed turbulence will laminarize when the rotation number is increased above 3. The validity of linear stability analysis based on the turbulent mean flow was investigated by Lezius & Johnston (1976), and by arguing that the turbulence scales are small and disordered they believed that the linear analysis could be valid. That would then also explain that the region of zero absolute mean-flow vorticity in the central part of the channel is governed by linear stability. The roll-cell-like structures are unsteady and will vanish when averaged in time and are, thus by definition, part of the turbulence. However, these structures will strongly influence the mean flow and cannot be considered as small or disordered and the validity of linear stability can be disputed. On the other hand, studies of rotating homogeneous turbulent shear flow have confirmed neutral stability for $Ro_l \approx 0.5$, see e.g. the numerical studies by Bardina, Ferziger & Reynolds (1983), Salhi & Cambon (1997) and Brethouwer (2005). The region of zero absolute vorticity was also addressed by Tanaka *et al.* (2000) by

stability analysis and by Yanase *et al.* (2004) using DNS and also Hamba (2006) using turbulence modelling arguments.

In the study performed by Grundestam *et al.* (2008), DNS of fully developed rotating channel flow were performed for a range of Ro up to 2.49. From this study, an increased damping of the turbulence kinetic energy can be seen for increasing Ro above 0.5. This is a monotonic trend that persists up to $Ro = 2.49$, which was the highest rotation number considered among the fully developed turbulent cases. Grundestam *et al.* complemented these turbulent simulations with a simulation initiated with a laminar flow with a superimposed perturbation and a system rotation rate set to give $Ro = 3.0$ for a laminar flow. An initial decay of this perturbation was indeed observed and this was interpreted as an indication that the flow should laminarize for some $Ro < 3.0$. Laminarization of strongly rotating flow was also observed from the DNS by Lamballais *et al.* (1996). However, streamwise waves, so-called Tollmien–Schlichting modes, are independent of rotation and it was found that these modes could start growing when all cross-flow modes (modes with non-zero spanwise wavenumber) were damped by rotation leading to a saturated state. Similarly, the cross-flow modes can be damped by a strong spanwise Lorentz force, resulting in a saturated state with high-amplitude spanwise-independent secondary flow, see Krasnov *et al.* (2008). These flows have close similarities with the simulation of two-dimensional channel flow transition by Jimenez (1990). In strongly rotating channel flow at higher Reynolds numbers, the high-amplitude instabilities may break down to three-dimensional turbulence that will be damped by the rotation. Such cyclic behaviour was observed numerically by Brethouwer, Schlatter & Johansson (2011).

The intention of the present study is to thoroughly investigate the details of the possible laminarization scenarios. First, we will address the laminarization process by linear stability mechanisms and also quantify the Reynolds number dependence of the critical rotation number by using linear stability analysis and DNS. Then, for supercritical Ro when the three-dimensional turbulence is suppressed, we will establish and study the saturated state with mainly two-dimensional large-amplitude secondary flow and eventually the breakdown to turbulence. In particular we will study how linear mechanisms govern both the laminarization of turbulence as well as the saturated supercritical state.

2. Method

2.1. *Governing equations and flow case setup*

Fully developed rotating channel flow is governed by the incompressible Navier–Stokes equations, i.e. conservation of momentum and mass for the instantaneous velocity and pressure fields: ($\tilde{u}_i = [\tilde{u}, \tilde{v}, \tilde{w}]$ and $\tilde{p}$)

$$\frac{\partial \tilde{u}_i}{\partial t} + \tilde{u}_j \frac{\partial \tilde{u}_i}{\partial x_j} = -\frac{\partial \tilde{p}}{\partial x_i} + \frac{1}{Re}\nabla^2 \tilde{u}_i + 2\epsilon_{ijk}\tilde{u}_j \Omega_k, \quad \frac{\partial \tilde{u}_i}{\partial x_i} = 0, \tag{2.1}$$

where ϵ_{ijk} is the permutation tensor. The variables are normalized by the channel half-width (δ) and the bulk velocity (U_b). Moreover, the centrifugal contribution is absorbed into the pressure.

The flow is homogeneous in the streamwise (x) and spanwise (z) directions and is rotating in the (x,y)-plane with the rotation vector $\Omega_i = \Omega \delta_{i3}$, see figure 1. The flow may be driven by a pressure gradient, or a volume force which is equivalent in incompressible flows. Alternatively, the flow may be driven by a constant mass or volume flux. Dynamically, these two approaches are different, in particular if

transitional flow events are present, like turbulence bursts. In the case of a pressure- or force-driven flow, the mass flow may then be reduced locally in time and the turbulent spot may be damped. Such events will probably have a more energetic development in mass- or volume-driven flows. In this study, the flow is driven by a constant pressure gradient in the x-direction, which is balanced by the wall skin friction $\tau_{wall} = \rho u_\tau^2$ in statistically steady flows. The wall skin-friction velocity is defined as

$$u_\tau = \sqrt{\nu \left| \frac{\mathrm{d}U}{\mathrm{d}y} \right|_{wall}}. \tag{2.2}$$

In rotating turbulent channel flows, the wall skin friction is, in general, unequal for the two walls and a quadratic mean is used,

$$u_\tau = \sqrt{(u_{\tau\text{-}p}^2 + u_{\tau\text{-}s}^2)/2}, \tag{2.3}$$

where $u_{\tau\text{-}p}$ and $u_{\tau\text{-}s}$ are the skin-friction velocities at the pressure (unstable) and suction (stable) sides, respectively. An alternative Reynolds number based on the skin friction is defined as

$$Re_\tau = \frac{u_\tau \delta}{\nu}. \tag{2.4}$$

For laminar flow, the solution is only a function of y, and is given by a rotation-independent parabola, $U(y) = 3(1 - y^2)/2$. Here, there is a simple relation between the two different Reynolds numbers, $3Re = Re_\tau^2$. In turbulent flows no such analytic relation exists and Re is, in general, smaller than in the case of laminar flow for a given pressure gradient or Re_τ.

2.2. *Linear stability theory*

The following linear stability analysis follows the work by Lezius & Johnston (1976). The classical transition scenario in channel flows is governed by exponential growth of unstable linear modes until turbulent breakdown occurs. Linear stability analysis is based on eigenanalysis of the Navier–Stokes equations linearized around the steady laminar base flow. The velocity and pressure fields are decomposed into the base flow and a small perturbation:

$$\tilde{u}_i = U_i(y) + u_i(\boldsymbol{x}, t), \quad \tilde{p} = P(x) + p(\boldsymbol{x}, t), \tag{2.5}$$

and since the flow is driven by a constant pressure gradient, the mean pressure is a linear function of the x coordinate. The centrifugal acceleration term due to system rotation is absorbed into the mean pressure $P(x)$.

The decomposition is then inserted into the Navier–Stokes equations (2.1) and the base solution is subtracted. The linearized equations for rotating channel flow in terms of the equations for the wall-normal velocity fluctuations v and the y-vorticity $\eta \equiv \partial u/\partial z - \partial w/\partial x$ are

$$\left[\left(\frac{\partial}{\partial t} + U\frac{\partial}{\partial x}\right)\nabla^2 - \frac{\mathrm{d}^2 U}{\mathrm{d}y^2}\frac{\partial}{\partial x} - \frac{1}{Re}\nabla^4\right] v = -Ro\left(\frac{\partial^2}{\partial x^2} + \frac{\partial^2}{\partial z^2}\right) u - Ro\frac{\partial^2 v}{\partial x \partial y}, \tag{2.6a}$$

$$\left[\left(\frac{\partial}{\partial t} + U\frac{\partial}{\partial x}\right) - \frac{1}{Re}\nabla^2\right] \eta = \left(Ro - \frac{\mathrm{d}U}{\mathrm{d}y}\right)\frac{\partial v}{\partial z}. \tag{2.6b}$$

The boundary conditions are $v = \partial v/\partial y = \eta = 0$ at the walls ($y = \pm 1$).

The equations together with the boundary conditions form a sixth-order eigenvalue problem. The solution is obtained by assuming wave-like solutions

$$u_i(\boldsymbol{x}, t) = \hat{u}_i(y)\mathrm{e}^{\mathrm{i}(\alpha x+\beta z-\omega t)}, \tag{2.7a}$$

$$\eta(\boldsymbol{x}, t) = \hat{\eta}(y)\mathrm{e}^{\mathrm{i}(\alpha x+\beta z-\omega t)}. \tag{2.7b}$$

Equation (2.6) can then be written as

$$\omega\left(\mathrm{D}^2-k^2\right)\hat{v} = \alpha\left(U\left(\mathrm{D}^2-k^2\right)-U''\right)\hat{v}+\frac{\mathrm{i}}{Re}\left(\mathrm{D}^2-k^2\right)^2\hat{v}+\beta Ro\hat{\eta}, \tag{2.8a}$$

$$\omega\hat{\eta} = \alpha U\hat{\eta}+\frac{\mathrm{i}}{Re}\left(\mathrm{D}^2-k^2\right)\hat{\eta}+\beta\left(U'-Ro\right)\hat{v}, \tag{2.8b}$$

where $\mathrm{D}\equiv \mathrm{d}/\mathrm{d}y$, $U'\equiv \mathrm{D}U$, $U''\equiv \mathrm{D}^2U$ and $k^2\equiv\alpha^2+\beta^2$. These are the Orr–Sommerfeld and Squires equations, which in the case of rotation ($Ro\neq 0$) form a fully two-way coupled system.

The other velocity components can be derived from $\hat{v}$ and $\hat{\eta}$ by using the incompressibility relation as

$$k^2\hat{u} = \mathrm{i}\alpha\mathrm{D}\hat{v}-\mathrm{i}\beta\hat{\eta}, \tag{2.9a}$$

$$k^2\hat{w} = \mathrm{i}\beta\mathrm{D}\hat{v}+\mathrm{i}\alpha\hat{\eta}. \tag{2.9b}$$

The equations are discretized in the y-direction by using Chebyschev polynomials with the aid of the MATLAB Chebyschev suite by Weideman & Reddy (2000). The eigenvalues (in terms of ω) and the corresponding eigenvectors (or eigenmodes) are found by solving the discrete generalized eigenvalue problem

$$\omega\boldsymbol{B}\boldsymbol{q} = \boldsymbol{A}\boldsymbol{q} \tag{2.10}$$

where

$$\boldsymbol{B} = \begin{bmatrix}\mathscr{D}^2-k^2 & 0\\ 0 & I\end{bmatrix}, \quad \boldsymbol{q} = \begin{Bmatrix}\hat{v}\\ \hat{\eta}\end{Bmatrix} \tag{2.11}$$

and

$$\boldsymbol{A} = \begin{bmatrix}\alpha\left(U\left(\mathscr{D}^2-k^2\right)-U''+\mathrm{i}Re^{-1}\left(\mathscr{D}^2-k^2\right)^2\right) & \beta Ro\\ \beta\left(U'-Ro\right) & \alpha U+\mathrm{i}Re^{-1}\left(\mathscr{D}^2-k^2\right)\end{bmatrix}. \tag{2.12}$$

Here, $\mathscr{D}$ is the discrete $\mathrm{d}/\mathrm{d}y$ operator.

3. Predictions by linear stability theory

3.1. *Neutral stability*

The DNS of rotating turbulent channel flow by Grundestam *et al.* (2008) is here used as the reference case. The channel flow is driven by a constant pressure gradient, thus the Reynolds number based on the friction velocity is constant and for the DNS it is $Re_\tau = 180$. The corresponding Reynolds number based on the bulk velocity is, however, dependent on the level of turbulence. In the limit of a laminar flow the Reynolds number is maximal and reaches $Re = 10\,800$, which is used for the present linear stability analysis.

For the given Reynolds number, the most unstable modes that give the highest critical rotation number are sought in the α–β plane. Figure 2(a) shows the critical

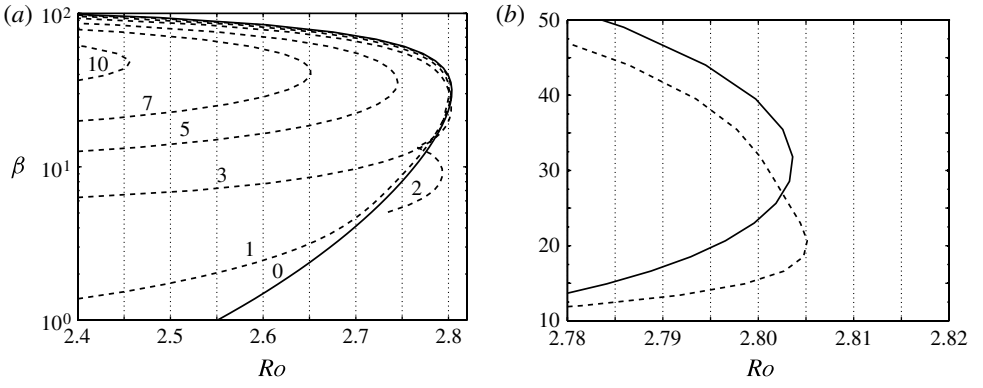

FIGURE 2. The neutral curves for different cross-flow modes for $Re = 10800$: (a) $\alpha = 0$ (—-), 1, 2, 3, 5, 7 and 10 (- - -, as marked in the figure) and (b) a zoom in to the two most amplified modes: I with $\alpha = 0$ (—) and II with $\alpha = 2.7$ (- - -).

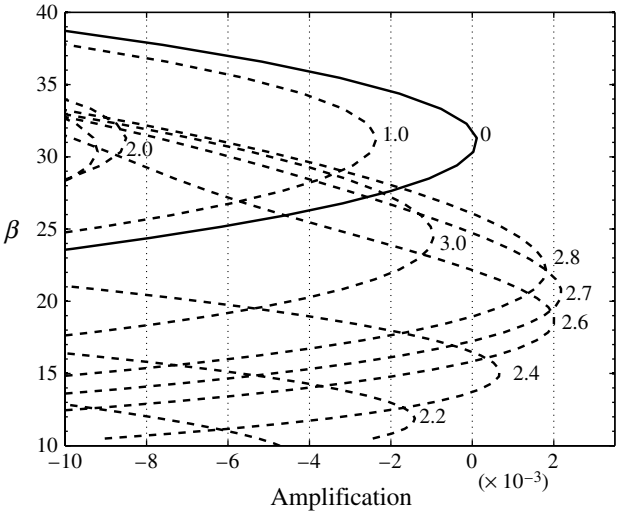

FIGURE 3. The amplification factor for $Ro = 2.799$ and $Re = 10800$ for $\alpha = 0$ (—), 1.0, 2.0, 2.2, 2.4, 2.6, 2.7, 2.8 and 3.0 (- - -, as marked).

rotation number as function of the spanwise wavenumber, β, for different streamwise wavenumbers, α. The most critical modes are found to be the steady roll cells aligned in the streamwise direction (mode I) and a slightly inclined unsteady mode (mode II). The neutral curves in terms of critical rotation number for different spanwise wavenumbers, β, are shown in figure 2(b) for these two modes. Mode I has a critical rotation number of $Ro_c = 2.803$ with $\alpha = 0$ and $\beta = 33$ while for mode II, $Ro_c = 2.805$ with $\alpha = 2.7$ and $\beta = 19$. Thus, the inclined mode is the most critical one. No cross-flow mode that is more critical has been found. Tollmien–Schlichting modes will be considered later in this section.

For $Ro = 2.799$, which is slightly below the critical rotation number for both mode I and II, the amplification factor should be positive for both these modes. This is verified in figure 3. It is also seen in the same figure that mode II is amplified for

a rather broad range of streamwise wavenumbers α between approximately 2.3 and 2.9 and that the maximum amplification rate is $\sim 2 \times 10^3$. The particular value of $Ro = 2.799$ corresponds to the least unstable DNS conducted within this study. The aim is to compare full nonlinear DNS with linearized methods close to the limit of vanishing turbulence.

3.2. *Reynolds number dependence*

To analyse the Reynolds number dependence of the critical rotation number and associated wavenumbers, we will first analyse the stability equations for Reynolds number approaching infinity. Equation (2.8) can then be written by eliminating $\hat{\eta}$ as

$$(\omega - \alpha U)^2 \left(\mathrm{D}^2 - k^2\right) \hat{v} + (\omega - \alpha U)\, \alpha U'' \hat{v} = \beta^2 Ro \left(U' - Ro\right) \hat{v}. \tag{3.1}$$

Moreover, we will assume that the governing mechanism is local so that the dependence on y can be expressed through the wavenumber γ and the ansatz (2.7) becomes $u_i(\boldsymbol{x}, t) = \hat{u}_i \exp[\mathrm{i}\,(\alpha x + \beta z + \gamma y - \omega t)]$. We then have

$$(\omega - \alpha U)^2 \hat{v} - (\omega - \alpha U)\, \frac{\alpha U''}{K^2} \hat{v} = \frac{\beta^2}{K^2} Ro \left(Ro - U'\right) \hat{v}, \tag{3.2}$$

where $K^2 \equiv \alpha^2 + \beta^2 + \gamma^2$.

First, for steady roll cells (mode I) $\alpha = 0$ and the second term on the left-hand side will vanish. This term can also be neglected for type II modes since $\alpha \ll K$. Then, the possibility of exponential growth of the solution is governed by the sign of the right-hand side and the solution is stable for $B^* = Ro(Ro - U') > 0$. $B^* = U'^2 B$ is directly related to the Bradshaw (1969) parameter B discussed in the introduction. The flow is a parabola, thus $U'(y) = -3y$ for $-1 \leqslant y \leqslant 1$. Assuming that locality in y holds, all type I modes are stable for $Ro > 3$, which is also approximately the critical rotation number for cross-flow modes of type II. This simplified analysis is in accordance with the non-local stability analysis in the previous section that gives $Ro_c \to 3$ as $Re \to \infty$.

The critical Ro that was found for $Re = 10\,800$ is significantly lower than the inviscid stability limit at $Ro = 3$. That means that there is a region close to the lower wall where the flow is inviscidly unstable but is probably stabilized by viscosity. Let us assume that the thickness d of this region is related to the wall viscous length scale so that $d^+ \equiv d u_{\tau-p}/\nu$ is reasonably constant for different Re. Also, we know that d^+ cannot be much larger than around 10 for significant viscous effects. An estimate of the critical rotation number, Ro_c, is then determined as $B^* = 0$ for $y = -1 + d$, or $Ro_c = U' = 3(1 - d)$. In terms of the wall viscous length scale $d = d^+/\sqrt{3Re}$, which gives

$$Ro_c = 3 - d^+ \sqrt{3} Re^{-1/2}. \tag{3.3}$$

The critical rotation number for $Re = 10800$ is $Ro_c = 2.805$, which gives $d^+ = 11.7$.

The simplified analysis gives that the critical rotation number will approach $Ro = 3$, for increasing Reynolds numbers, as $Re^{-1/2}$ because of vanishing viscous effects. The Reynolds number dependence was investigated by computing the neutral curves for Reynolds numbers ranging from 10^3 to 10^6 corresponding to $Re_\tau = 55$–1732. For each Reynolds number, the most critical mode was identified. Mode II ($\alpha \neq 0$) is the most critical for all investigated Reynolds numbers except for the lowest ($Re = 10^3$) where mode I, steady roll cells, is the most critical one. The deviation from $Ro = 3$ is plotted in figure 4 in terms of $1/(3 - Ro_c)$ and remarkably closely follows a power law for all

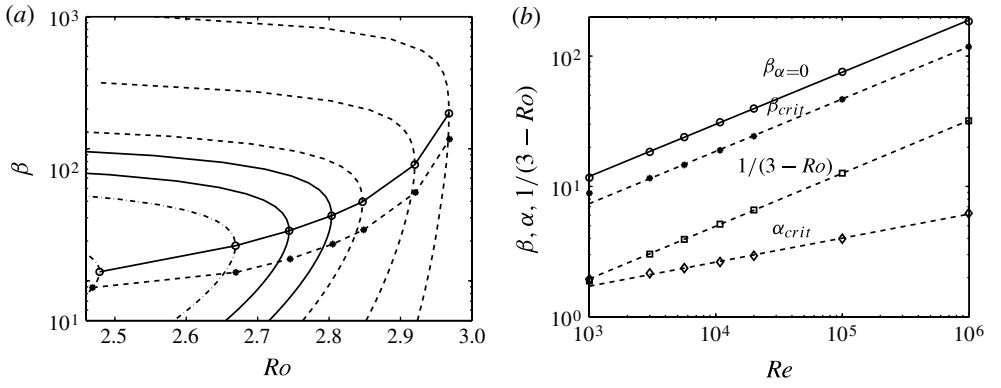

FIGURE 4. (*a*) The neutral curves for stationary modes ($\alpha = 0$) for $Re = 1000$, 3000, 5633, 10 800, 20 000, 10^5, 10^6 from left to right. The largest Ro and corresponding critical β for each Re is shown as ○ with a connected line, and the most critical Ro for $\alpha \neq 0$ is shown as ● with a connected dashed line. (*b*) The critical α (◇), β (●) and Ro (□) (as $1/(3 - Ro)$) versus Re with symbols for the same Re cases as in (*a*) and the lines representing the least-squares fit to the data. Also the most critical β (○) for $\alpha = 0$ is shown.

but the lowest Reynolds number. A linear least-squares fit, excluding $Re = 10^3$, gives

$$Ro_c = 3 - 8.40Re^{-0.405}. \tag{3.4}$$

A relation for the thickness of the viscous layer is obtained by relating the least-squares fit to the simplified analysis in (3.3), which gives $d^+ = 4.85Re^{0.095}$. The evaluated d^+ has a small, but significant, Reynolds number dependence and will vary between 9 and 18 for Re from 10^3 to 10^6. Thus, d^+ is in the range where viscous effects are expected to be of importance. However, the difference in the Reynolds number dependence indicates that there could be additional mechanisms not considered in the simplified analysis. However, it can be concluded that the simplified analysis, in general, is supported by the numerical data.

The corresponding critical wavenumbers, α and β, increase with increasing Reynolds number and a linear fit gives $\alpha_c = 0.475Re^{0.185}$ and $\beta_c = 0.453Re^{0.402}$. Also here the lowest Reynolds number is excluded from the fit. The spanwise wavenumber β is related to the size of the structures, and with the assumption that the structures must exist within the unstable near-wall region then $\beta_c \sim 1/d \sim Re^{1/2}$. The critical streamwise wavenumber is not directly related to the wall-normal extent of the near-wall region, resulting in a weaker Reynolds number dependence compared with the critical wall normal and cross-flow wavenumbers.

3.3. *Tollmien–Schlichting modes*

The stability analysis shows that all cross-flow modes are stable for rotation numbers greater than 3. However, by inspecting the Orr–Sommerfeld equation (2.8), the terms containing the rotation number are all multiplied by the spanwise wavenumber β and with $\beta = 0$ the influence of rotation is broken. Modes with $\beta = 0$ are the so-called Tollmien–Schlichting (TS) modes which, thus, are independent of rotation. The Reynolds number used in the DNS study is larger than the critical Re for channel flow, and unstable TS modes will exist. Figure 5(*a*) shows the amplification rate for different streamwise wavenumbers (α) for plane TS modes ($\beta = 0$) and inclined modes with β ranging from 0.1 to 2.0. A slight increase in α rapidly damps the TS mode and

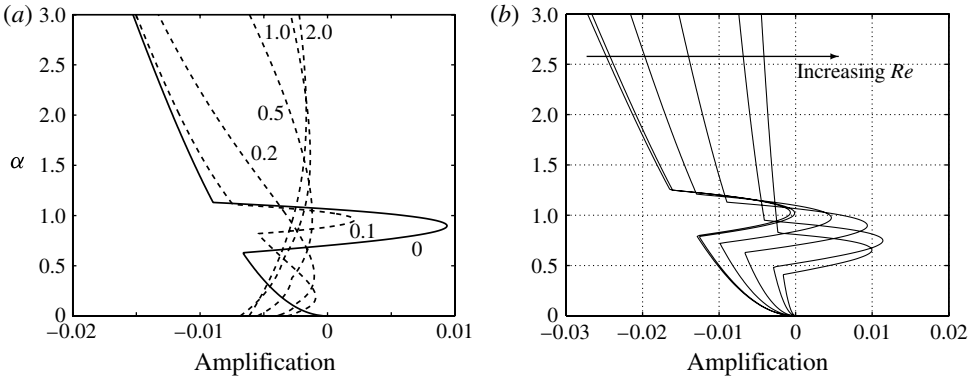

FIGURE 5. The amplification factor for TS modes. (*a*) Amplification factor for $Ro = 2.80$, $Re = 10800$ and small $\beta = 0$ (—), 0.1, 0.2, 0.5, 1.0 and 2.0 (- - -, as marked). (*b*) The amplification factor for TS waves ($Re_\tau = 105$, 107.4, 130, 180, 360 and 590 from left to right in the upper part of the figure).

there is only a narrow interval in α where the TS modes are unstable. The influence on the Reynolds number is shown in figure 5(*b*) where the critical streamwise wavenumber α decreases with increasing Re and the corresponding unstable α interval will change. The critical Reynolds number for the TS modes found by Orszag (1971) and Lakin *et al.* (1978) corresponds to $Re_\tau = 107.4$, which is verified in this figure showing a maximum amplification factor close to zero.

The breakdown to turbulence for the TS modes in the rotating case will be different from the breakdown in non-rotating channel flow. The reason is that the secondary modes that are generated in the pre-transitional phase will have $\beta \neq 0$, and then the coupling terms in the Orr–Sommerfeld equation (2.8) will be activated. For $Ro > Ro_c$ these modes will be linearly stable and the mechanisms for activating the secondary modes must be nonlinear.

TS waves are known to be stabilized by nonlinear streamwise vortices (see e.g. Fransson *et al.* 2005; Bagheri & Hanifi 2007) and therefore TS modes are not easily activated in turbulent flows. Also, the growth rate of the TS modes is almost two orders of magnitude lower (<1 %) than that for the most amplified roll cells. However, for rotation rates larger than critical, the TS waves have the possibility of growing after the other disturbances have reached sufficiently low amplitudes. This will be further discussed later in relation to the corresponding numerical simulation.

4. Simulations

Direct numerical simulations have been performed to confirm the predictions from linear stability theory and further investigate the behaviour in the finite-amplitude, nonlinear, regime. All simulations were performed with the pseudo-spectral flow solver by Lundblad, Henningson & Johansson (1992). It is based on the velocity–vorticity formulation and solves for the wall-normal vorticity and the Laplacian of the wall-normal velocity. In this formulation, the fluctuating pressure is eliminated from the governing equations and hence no pressure solver is needed during the simulation. Fourier series expansions are used in the periodic streamwise and spanwise directions (x and z) while Chebychev series are used in the wall-normal direction (y). Time integration is done using a Crank–Nicolson scheme for the linear terms and a four-

Re	Re_τ	$n_x \times n_y \times n_z$	L_x/δ	L_z/δ	Init
3675	105	$120 \times 97 \times 96$	4π	2π	ini
3675	105	$240 \times 97 \times 96$	8π	2π	ext
5633	130	$120 \times 161 \times 96$	3π	1.5π	ini
10800	180	$192 \times 201 \times 160$	3π	1.5π	ini
10800	180	$192 \times 201 \times 160$	4π	2π	ini
10800	180	$384 \times 201 \times 160$	16π	2π	ext
10800	180	$384 \times 201 \times 160$	8π	2π	ext
10800	180	$384 \times 201 \times 320$	8π	8π	ext
10800	180	$192 \times 201 \times 160$	8π	8π	ext
10800	180	$384 \times 201 \times 160$	8π	4π	ext
10800	180	$384 \times 201 \times 320$	16π	16π	ext
10800	180	$96 \times 201 \times 96$	4π	4π	ini

TABLE 1. Simulation parameters: n_i indicates the resolution in direction i, L_x and L_z denote the size of the computational box in the streamwise and spanwise directions, and Init denotes the type of initialization, explained in the text.

stage Runge–Kutta method for the nonlinear terms. The flow in all simulations is driven by a constant pressure gradient. In this way the value of Re_τ is predetermined for the fully developed flow.

Simulations were done for three different Reynolds numbers, $Re_\tau = 105$, 130 and 180, for a series of rotation numbers in the critical regime of each Reynolds number. Depending on the purpose of the simulations, different sizes of computational domains have been used. These are listed in table 1 where L_x/δ and L_z/δ denote the streamwise and spanwise lengths of the computational box in terms of the channel half-width, respectively. $n_x \times n_y \times n_z$ denotes the resolution in the streamwise, wall-normal and spanwise direction, respectively. The purpose of these simulations will be further discussed in the two sections below.

Simulations presented in § 5, indicated with 'ini' in table 1 in the column 'Init', were initialized using the following procedure. First, a fully developed non-rotating turbulent channel flow was obtained, initiated with a velocity field consisting of a parabolic profile with a pair of streamwise counter-rotating vortices described by Henningson, Lundbladh & Johansson (1993). Then, the system rotation was gradually increased step by step. After each increase in system rotation, the solution was advanced long enough in time to attain a statistically steady state. This was especially important when the critical Ro-regime was approached since the rotation number is, for a particular system rotation, determined by the bulk velocity, which in turn is the quantity that requires the largest number of iterations to attain its steady-state value. Statistically steady-state solutions were obtained for all subcritical Ro.

The simulations presented in § 6 with streamwise box lengths of $8\pi\delta$ and $16\pi\delta$ were, on the other hand, initialized by extending the velocity field from the corresponding $4\pi\delta$-simulation. These are marked 'ext' in the 'Init' column of table 1.

5. Critical Ro and structures

Linear stability is usually only indicative concerning the critical condition for transition to turbulence and, in particular, concerning laminarization of turbulent flow. Typically, the transition to turbulence occurs at Reynolds numbers lower than those at which linear instabilities first appear. Plane Couette and pressure-driven circular pipe

Re	Re_τ	Ro_u	Ro_s	Ro_c
3675	105	2.690	2.710	2.698
5633	130	2.722	2.752	2.746
10800	180	2.799	2.811	2.805

TABLE 2. Unstable and stable Ro obtained through simulations. Ro_c denotes critical Ro predicted by linear stability analysis.

flows are extreme in this sense since these flows are linearly stable for all Reynolds numbers. Still transition to turbulence occurs in these flows even in situations with minimal initial perturbations. Laminarization of turbulent flow is usually even less related to linear stability and turbulent flow may persist for Reynolds numbers lower than those at which transition to turbulence first occurs.

The turbulence in fully developed channel flow has been found to be strongly damped by spanwise rotation. The previous study by Grundestam *et al.* (2008) indicated that complete laminarization of the flow may be closely related to the critical rotation number, $Ro < 3$, for which cross-flow modes may become linearly unstable. In this section we will verify that the laminarization of fully developed turbulent channel flow is governed by linear mechanisms and that the critical rotation number, Ro_c, derived in the previous section can be verified also in the nonlinear case studied by DNS.

The governing mechanism in the laminarization process is the stabilization of the cross-flow modes by rotation. TS modes are, however, always unstable for $Re_\tau > 107$, but will be damped by the nonlinear turbulence. When approaching the critical rotation number, Ro_c, the TS modes may start growing when the turbulence is damped below some critical level. Neither the critical rotation number Ro_c nor the flow structures and statistics near Ro_c can be studied when the TS modes are active. For this reason, the unstable TS mode will be artificially disabled in the first part of the study. Hence, the streamwise box size was chosen to be $3\pi\delta$ in order not to allow the presence of the amplified TS wave in the solution with $\alpha \sim 1$, see figure 5, since the resolved streamwise wavenumbers will be $\alpha = 2n/3$, where n is an integer. Hence, no discrete α modes will be present within the range of unstable streamwise wavenumbers for $Re_\tau \leqslant 180$ among the Reynolds numbers studied in figure 5. Here, we will use $Re_\tau = 180$, 130 and 105, see table 2. The case with $Re_\tau = 105$ was chosen due to the stable character of all TS modes. Hence, no further restriction of the computational box is needed and a 4π box is used for that case.

5.1. *Reynolds number dependence of critical Ro*

The critical rotation number, Ro_c, is determined for each Reynolds number by increasing Ro step by step from a fully turbulent state until the flow laminarizes. The results from the simulations are consistent with the predictions made by linear stability theory. The pre- and post-critical rotation numbers, Ro_u and Ro_s respectively, obtained in the DNS, are given in table 2 together with the critical rotation numbers obtained from linear stability analysis. The results are also illustrated in figure 6 where figure 6(*a*) is a graphical representation of table 2 where predictions made by linear theory for a range of Re are included. Figure 6(*b*) displays additional information about the bulk velocity as function of Ro, obtained through the preceding simulations at lower Ro and from Grundestam *et al.* (2008). The value of U_b/U_b^{lam} approaches

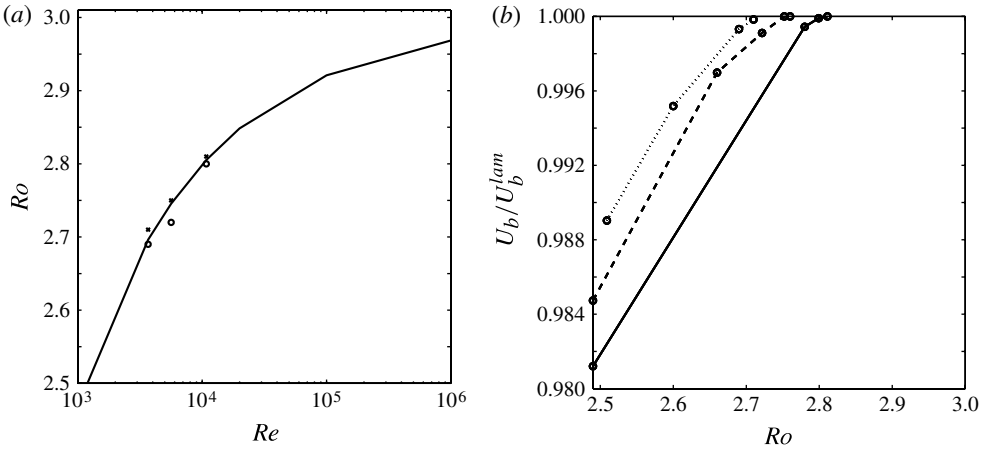

FIGURE 6. (*a*) Ro_c as a function of Re from stability analysis (—), and simulations for Ro_u (○) and Ro_s (×). (*b*) Normalized U_b as a function of Ro for $Re_\tau = 180$ (—), 130 (- - -) and 105 ($\cdots$), where each symbol represents one DNS.

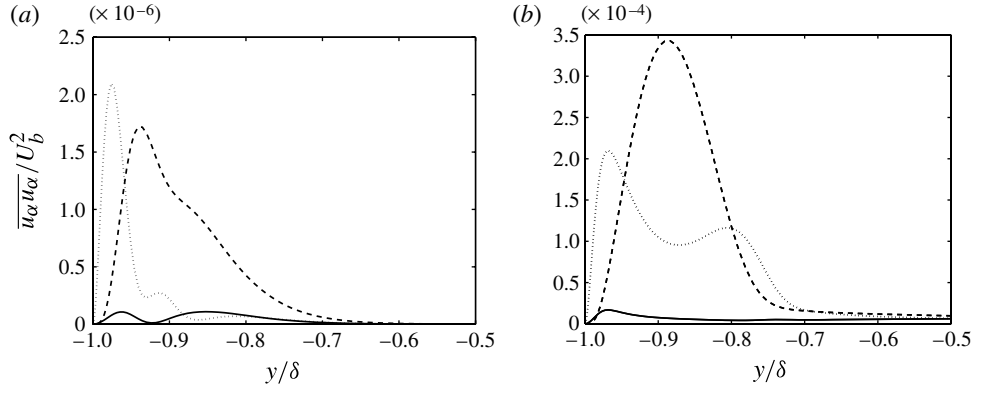

FIGURE 7. Normalized Reynolds stresses for (*a*) $Ro = 2.799$ and (*b*) $Ro = 2.49$: $\overline{uu}/U_b^2$ (—), $\overline{vv}/U_b^2$ (- - -) and $\overline{ww}/U_b^2$ ($\cdots$).

unity when the flow becomes laminar and one can note the gradual laminarization for increasing Ro. U_b^{lam} is defined as the bulk velocity for a particular Re_τ and is related to u_τ as $U_b^{lam} = Re_\tau u_\tau/3$. The results clearly demonstrate that the critical rotation number is dependent on the Reynolds number, an issue that was merely touched upon by Grundestam *et al*. It should be pointed out that the critical rotation numbers derived from linear stability are extremely well captured by the DNS with an accuracy of $\sim$1 %. Moreover, it should be emphasized that the rotation number was increased step by step, starting from a non-rotating fully developed turbulent state, until the flow laminarizes. Hence, the DNS not only confirms the linear stability analysis, but also shows that the nonlinear turbulent flow will laminarize according to the critical rotation number given by linear stability.

When the results from the simulations are analysed for subcritical values of Ro, the flow solution shows many of the characteristics that can be seen for much smaller Ro. For example, the $\overline{uv}$-profile is negative in a region close to the wall on the pressure side of the channel and the wall-shear velocity is higher on this side. In figure 7 where

the diagonal Reynolds stresses are shown, the same type of behaviour can be seen as in the previous simulations for lower Ro by Grundestam *et al.* (2008). The part of the domain where $y/\delta \geqslant -0.5$ is not shown since the Reynolds stress levels are small in comparison to those close to the wall at $y/\delta = -1$. As a comparison, the diagonal Reynolds stresses for the case of $Ro = 2.49$, from Grundestam *et al.* are displayed in figure 7(*b*). Note that the peak value of $\overline{vv}/U_b^2$ is a factor of $\sim$200 times larger for $Ro = 2.49$ than the corresponding value for $Ro = 2.799$ in figure 7(*a*). Despite this difference in magnitude the character of the stress distributions is rather similar for the two cases. The two flow cases are fundamentally different. At $Ro = 2.49$ the flow can be seen as fully turbulent. The case of $Ro = 2.799$, on the other hand, has structures of rather different character. This is further discussed in the section below.

For supercritical Ro the simulation shows a flow which has essentially laminar features, e.g. equal skin-friction velocities on the two sides of the channel, the mean velocity profile is close to that of the laminar flow and the Reynolds stresses are negligible. It is also evident from the simulations that once the rotation number has been increased to supercritical values, the time scale of the laminarization process is relatively short.

The particular box size, $3\pi\delta \times 2\delta \times 1.5\pi\delta$, used in this simulation allows the existence of modes with $\alpha = 2n/3$ and $\beta = 4m/3$ where n and m are integers. Hence, no mode in the simulation exactly matches the most critical modes of $(\alpha = 2.62, \beta = 19)$ and $(\alpha = 0, \beta = 33)$ obtained with the linear analysis. The closest numerical modes are $(\alpha = 2.67, \beta = 18.66)$ and $(\alpha = 0, \beta = 33.33)$ respectively. This is discussed further below. Moreover, the box width of $1.5\pi\delta$ was found sufficient by verifying relaminarization of the turbulent state at $Ro = Ro_c$ by the use of larger ($3\pi\delta$ and $6\pi\delta$) spanwise box sizes.

5.2. *Structures and eigenmodes*

The two most critical modes, I and II, for $Ro = 2.799$ from the linear stability analysis are here further investigated. The rotation number is reduced to $Ro = 2.49$ while keeping the critical wavenumbers α and β constant in order to have a strong amplification of these modes. The chosen wavenumbers may, however, not be the most amplified for the lower rotation rate. Analysis of these modes at $Ro = 2.49$ shows two amplified eigenmodes (positive imaginary values) for each mode, see figure 8. Mode I has the largest amplification factor of over 0.5. The real value of these eigenvalues is zero corresponding to a pure amplification without harmonic content. The amplification rate for mode II, which has the highest critical rotation number, is slightly lower. This implies that the most critical mode is not the most amplified for this lower rotation number. The real value of the unstable eigenvalues for mode II is non-zero indicating that these modes are not stationary in space. The amplification rate for the most unstable modes is remarkably high. A growth rate of 0.5 implies that the amplitude is doubled in less than $1.4\delta/U_b$ time units. For $Ro = 2.799$, on the other hand, there is just one amplified eigenmode for each critical mode and the amplification factors are much lower than for $Ro = 2.49$. The non-stationary nature of the II mode also applies for $Ro = 2.799$.

It is interesting to compare the flow field obtained from the finite-amplitude simulations with the physical properties of the unstable eigenmodes. From figure 7 it is clear that the streamwise velocity fluctuations in the DNS have the smallest magnitude. It can also be noted that the spanwise fluctuations are significant only in a narrow region close to the wall and that the streamwise velocity fluctuations are at least one order of magnitude smaller. Thus, the wall-normal velocity plotted in

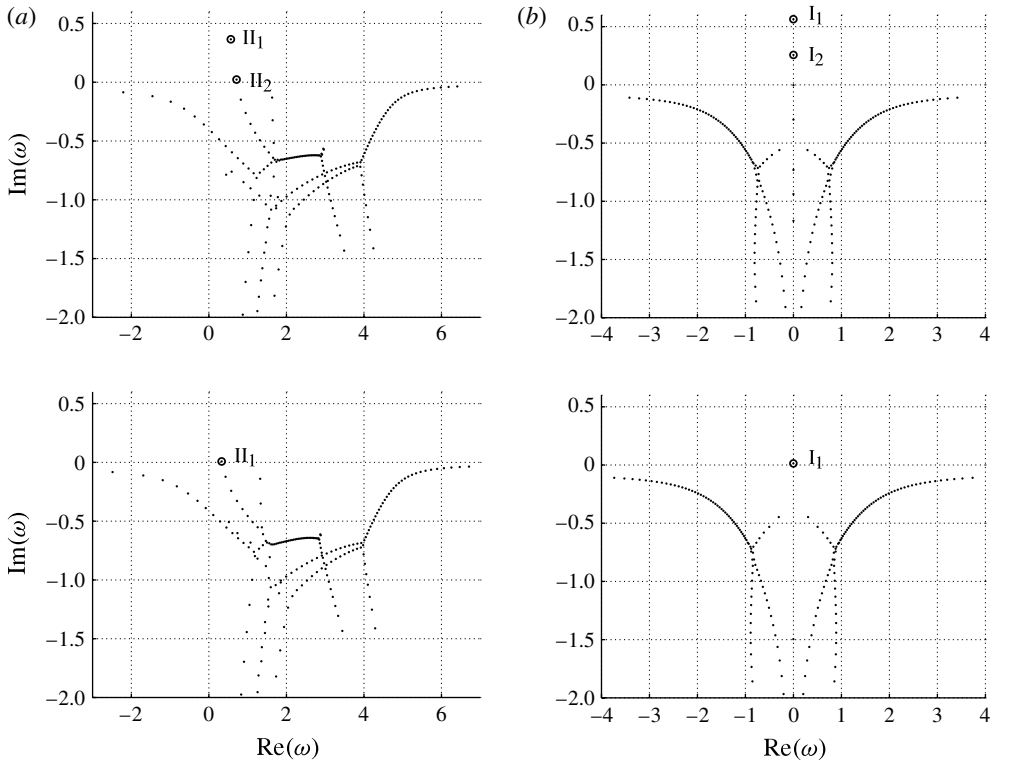

FIGURE 8. (*a*) Eigenmodes for the critical $\alpha = 2.63$ and $\beta = 19.0$ and (*b*) the most amplified $\alpha = 0$, $\beta = 33.0$ eigenmodes, at $Ro = 2.49$ (top) and $Ro = 2.799$ (bottom) for $Re = 10\,800$.

(y, z)-planes should serve well to illustrate the flow, as shown in figures 9 and 10 for $Ro = 2.49$ and 2.799, respectively. For $Ro = 2.49$, the first and second eigenmodes of mode I (I_1 and I_2) are one and two layers of roll cells. The oblique vortices of mode II are visible in the (y, z)-plane as tilted roll cells and the second eigenmode (II_2) is more tilted than the first (II_1). The modal shape from the linear analysis can be compared with the fully developed nonlinear DNS study of Grundestam *et al.* (2008) for the same *Ro*. The simulation shows streamwise structures that are almost periodical in the spanwise direction, see figure 9(*c*). Oblique structures similar to the mode II first eigenmode (II_1) can be seen and also smaller straight structures similar to the mode I first eigenmode (I_1), which is the eigenmode with the highest amplification of the I modes, are visible. Also the second eigenmode of mode I (I_2) can just barely be seen as triple dots at a few places. Furthermore, the spanwise wavelength and the wall-normal extension of the structures of the simulation are comparable to those of the eigenfunctions from the stability analysis. The second eigenmode of mode II (II_2), which has the lowest amplification rate, cannot be identified in the DNS field.

For $Ro = 2.799$, the analysis reveals two eigenmodes of interest, I_1 and II_1. Each eigenmode consists of one layer of roll cells. Mode II_1 is slightly tilted and extends further away from the wall. The resemblance between the physical flow and the eigenmodes from the stability analysis is striking. In fact, to the eye the simulated flow looks like a blend of the eigenmodes from the stability analysis. From this point of view, the case of $Ro = 2.799$ is very different from that of $Ro = 2.49$, where

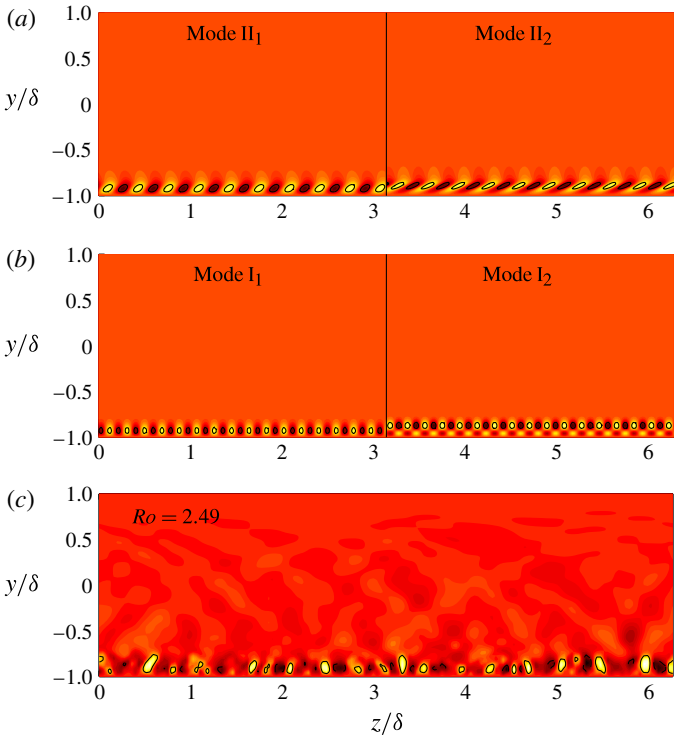

FIGURE 9. Wall-normal velocity fluctuations for (*a*) the eigenmode with the critical $\alpha = 2.63$ and $\beta = 19.0$ (II), and (*b*) the most amplified eigenmodes at $Ro = 2.49$ ($\alpha = 0$, $\beta = 33.0$) (I), and (*c*) from a corresponding snapshot of the DNS by Grundestam *et al.* (2008) at $Ro = 2.49$ and $Re = 10\,800$.

many more wavenumbers are excited, see figure 9. Furthermore, figure 7 shows that for $Ro = 2.49$ fluctuations are not only localized to a region close to the wall on the pressure side of the channel, but are present in a region extending beyond the centreline of the channel.

As the rotation number is increased towards the critical regime, it seems reasonable to assume that more and more modes will become stable and therefore contain less and less energy. Consequently, at rotation number $Ro = 2.799$, just slightly below the critical Ro only the modes of positive amplification, shown in figure 3, should contain significant amounts of energy.

Of the unstable modes shown in figure 3 for $Ro = 2.799$, the dimensions of the computational box used in the present simulations allow modes of streamwise wavenumbers $\alpha = 0$ and 2.67 only. Thus, modes within the regime of $15 \lesssim \beta \lesssim 24$ with $\alpha = 2.67$ are linearly unstable and can be expected to be active in the DNS. In order to study the active modes, (α, β)-planes in Fourier space are considered where the Fourier components of the kinetic energy have been integrated in the wall-normal direction. Complementary information regarding the wall-normal energy distribution is provided through figure 7. Figure 11 shows the integrated energy in Fourier α–β space for $Ro = 2.799$ and $Ro = 2.49$. The domain in the plot has been restricted to where significant amounts of energy are present for $Ro = 2.799$. A first inspection reveals extensive differences between the two cases. For $Ro = 2.799$, all energy is contained in

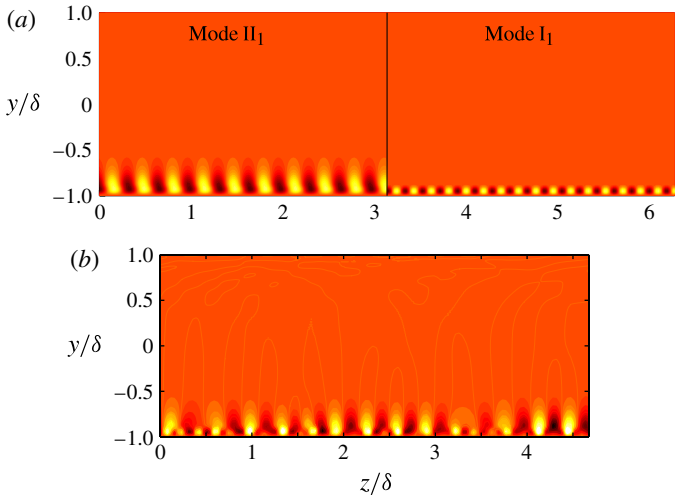

FIGURE 10. Wall-normal velocity fluctuations for (*a*) the eigenmode with the critical $\alpha = 2.63$ and $\beta = 19.0$ (II_1, left) and the most amplified eigenmodes at $Ro = 2.799$ ($\alpha = 0$, $\beta = 33.0$) (I_1, right) and (*b*) from a corresponding snapshot of the DNS by Grundestam *et al.* (2008) at $Ro = 2.799$ and $Re = 10\,800$.

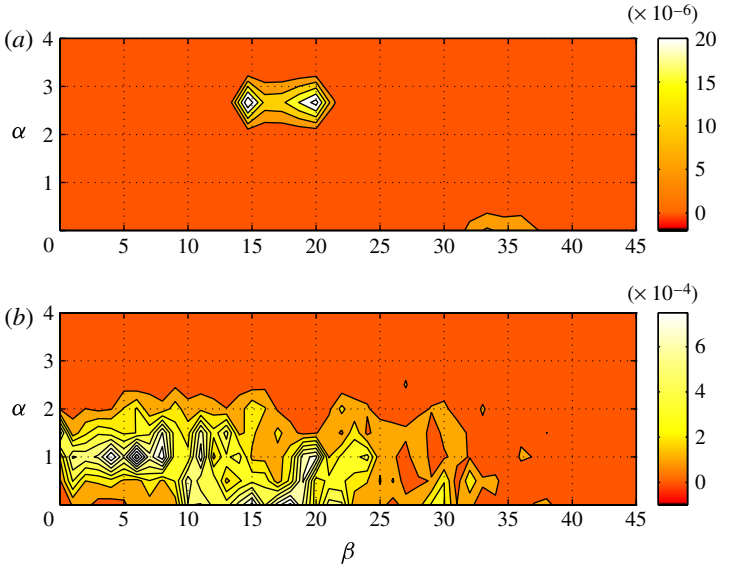

FIGURE 11. Contour plot of the total *y*-integrated energy in the Fourier (α, β)-plane for (*a*) $Ro = 2.799$ and (*b*) $Ro = 2.49$, normalized by the mean flow kinetic energy.

two areas corresponding to the I_1 and II_1 modes. For $Ro = 2.49$, on the other hand, a large number of modes are excited. One can also note that a wider range of β is active than for α. It should be noted that the amplitudes are much lower for $Ro = 2.799$ than for $Ro = 2.49$ in figure 11 and for plotting conveniences the colour coding and isolines are not the same.

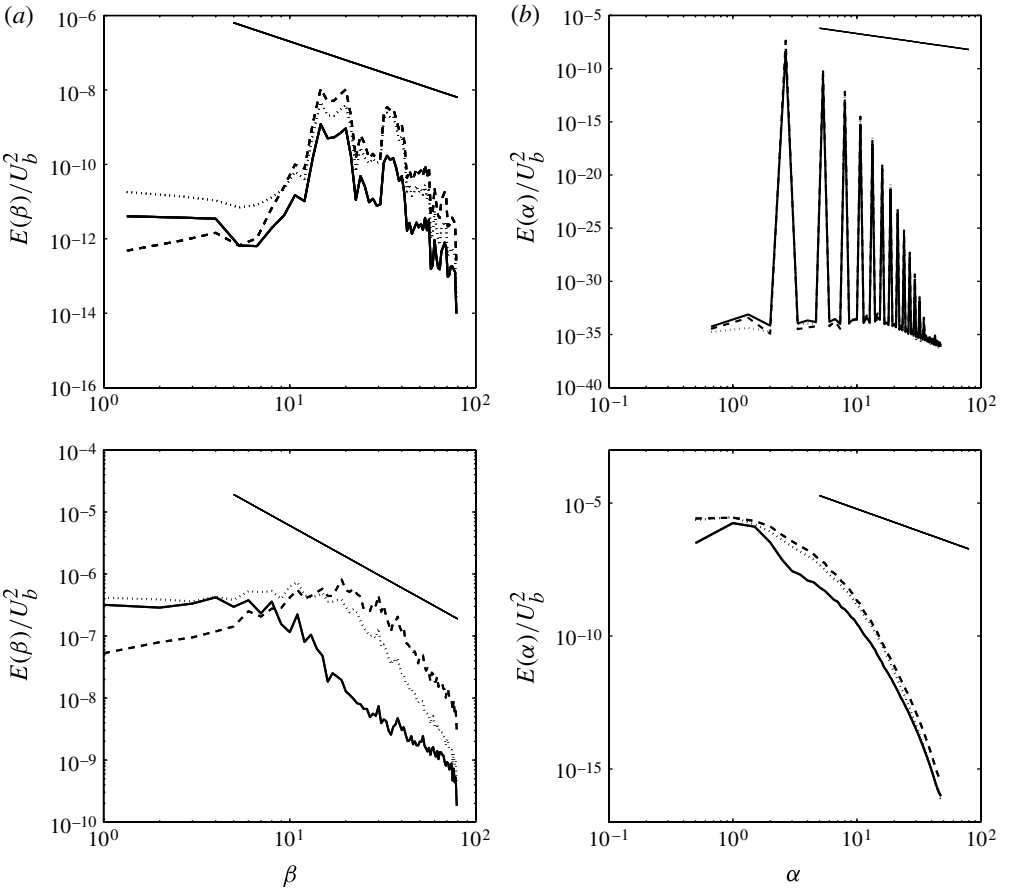

FIGURE 12. Normalized component-wise energy spectra E/U_b^2 for summation in (a) the streamwise and (b) spanwise Fourier directions for $Ro = 2.799$ (upper) and $Ro = 2.49$ (lower): E_{11}/U_b^2 (—), E_{22}/U_b^2 (- - -) and E_{33}/U_b^2 ($\cdots$); $-5/3$-slope marked with a straight line.

In order to further investigate the flow, energy spectra were investigated. The anisotropic character of the flow implies that studying the turbulence spectrum as a function of total wavenumber, $K^2 = \alpha^2 + \beta^2 + \gamma^2$, is not adequate. In fact, for channel flow no two directions are equal from a statistical point of view. The walls impose a strong effect on the anisotropy in addition to the effect the pressure-gradient-driven mean flow has on the turbulence. Therefore, it seems reasonable to study spectra which are functions of one of the two spectral directions, α and β, while summing over the other.

The Fourier components have been integrated in the wall-normal direction and the corresponding spectra are shown in figure 12 for $Ro = 2.799$ and 2.49. The two regions around the unstable I_1 and II_1 modes ($\beta = 33$ and 19) are easily distinguishable for $Ro = 2.799$ in figure 12(a). One can also note that in analogy with figure 7, the wall-normal component carries the largest amount of energy while the streamwise carries the smallest. For $Ro = 2.49$ the corresponding plot in figure 12(a) shows a more smooth variation of the distributed energy consistent with turbulent flow where the largest structures carry the major part of the energy.

The spectrum for $Ro = 2.799$, where summation over the spanwise wavenumbers has been applied, clearly demonstrates the uniqueness of the instability of the II_1 mode with a distinct peak at $\alpha = 2.67$. Peaks are also seen for wavenumbers that are multiples of $\alpha = 2.67$ with decreasing amplitude for increasing α. It seems plausible that they represent the cascade of the II_1 mode energy to modes of higher harmonics. The presence of multiples of α is simply a result of the nonlinear interaction in the Navier–Stokes equations. The corresponding spectrum for $Ro = 2.49$ is of completely different character and shows a smooth behaviour with a monotonically decreasing amplitude for increasing α.

All in all, this indicates that for $Ro = 2.799$ the flow does not possess the spectral properties of a turbulent flow. Instead, a small number of modes are unstable and only these contribute with fluctuations of significant energy.

6. Saturated states with extreme-amplitude waves

In the previous section, the destabilizing effect of the TS modes was artificially excluded by choosing the streamwise box length such that the unstable TS modes could not exist in the computational box. In this section we perform simulations where we also capture the unstable TS waves by using a computational box that allows the existence of the linearly unstable $\alpha = 1$ mode. This computational box was given the dimensions $8\pi\delta \times 2\delta \times 8\pi\delta$, which allows streamwise and spanwise wavenumbers as multiples of 0.25. The simulation was performed for $Re_\tau = 180$ and a rotation rate that gives $Ro = 3.0$ for the corresponding laminar parabolic profile.

A precursor simulation, based on the statistically steady $Ro = 2.66$ case, was computed using the $4\pi\delta \times 2\delta \times 2\pi\delta$ box. Then, Ro_{lam} was increased to 3.0 leading to an initial laminarization followed by the growth of the unstable TS waves. In the analysis of the high-amplitude state we will introduce the Reynolds decomposition of the velocity field into a mean and a fluctuating part, $\tilde{u}_i = U_i + u_i$, where the fluctuating part in this case will carry the nonlinear fluctuations in contrast to the definition in (2.5). Moreover, the different modes will be identified by their (α, β) combination.

Due to the existence of unstable α modes in the solution, the flow behaviour in this simulation is fundamentally different from that observed for the computational box of length $3\pi\delta$ in which no unstable α modes exist. The time evolution of the flow is illustrated in figure 13 by the energy of the most energetic modes at $y/\delta = 0.72$. Figure 13(a) shows the complete simulation and figure 13(b) is zoomed in around the second peak. The integrated energy in the y-direction shows basically the same behaviour. Also shown in the figure are the total kinetic energy of the fluctuations, K, and the turbulence kinetic energy, K_{nonrot}, for the corresponding non-rotating channel with the same pressure gradient (same U_b^{lam}).

Initially, the flow is dominated by the growth of the $(1, 0)$ mode ($\alpha = 1$ and $\beta = 0$) until extremely large amplitudes are reached. Since almost all energy is contained in the $(1, 0)$ mode, it cannot be distinguished from K in the figure. The maximal magnitude of the energy content is extremely high, almost two orders of magnitude higher than the turbulence level in the corresponding fully developed non-rotating turbulent channel flow, K_{nonrot} in the figure. The streamwise wavenumber for the most amplified mode in the linear limit is about $\alpha \approx 0.9$ according to figure 5. During the initial linear growth the $\alpha = 1.0$ mode is the most amplified among the modes that can be captured within the 8π computational box, i.e. with steps of $\Delta\alpha = 1/4$. The importance of the box size will be discussed at the end of this section. The extreme amplitudes persist for periods of roughly 100 time units, whereafter the flow starts to

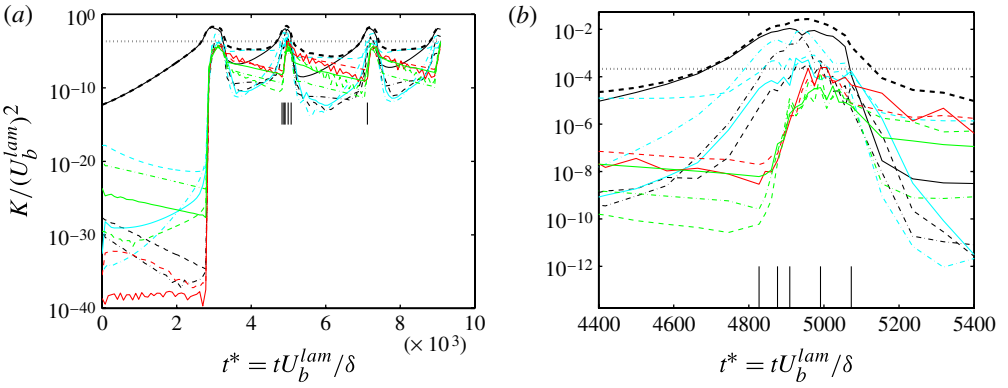

FIGURE 13. Energy for various modes at $y/\delta = 0.72$, box size $8\pi\delta \times 2\delta \times 8\pi\delta$. (*a*) The total time of the simulation. (*b*) A close-up around the second peak in (*a*). Thick black curves: total fluctuation energy K for the present case (- - -) and corresponding non-rotating turbulent case ($\cdots$). Thin black curves: $\beta = 0$ modes with $\alpha = 1.0$ (—), 0.5 (- - -) and 1.5 (-··-). Light blue curves: additional $\beta = 0$ modes with $\alpha = 0.25$ (—), 0.75 (- - -) and 1.25 (-··-). Red curves: $\beta = 0.25$ modes with $\alpha = 0.25$ (—) and 0.5 (- - -). Green curves: $\beta = 0.5$ modes with $\alpha = 1.0$ (—), 0.5 (- - -) and 1.5 (-··-). See figure 14 for explanation of the vertical lines.

break down and eventually laminarizes. When all disturbances have been damped to very low levels, the $(1, 0)$ mode starts to grow again and the extreme-amplitude state and breakdown is repeated quasi-periodically. The period time is extremely long, of the order of 2000 time units, which corresponds to around 50 times of flow through the $8\pi\delta$ box.

6.1. *Periodic breakdown*

The breakdown from the extreme-amplitude state will be further analysed. We will start by visualizing the fluctuating streamwise velocity in figure 14, showing coloured contour plots of (x, z)-planes at the wall-normal position, $y/\delta = 0.72$. The first five snapshots are taken closely in time around the second peak in figure 13 and the last one just before the third peak. These times are indicated in figure 13 as vertical lines.

In the first snapshot, for $t^* = 4827$, we clearly see the high-amplitude $(1, 0)$ mode with a small modulation by the $(1.25, 0)$ mode, which is also visible in figure 13. The early signs of influence of oblique modes can be seen in the second snapshot and in the third snapshot, for $t^* = 4909$, large-amplitude three-dimensional structures are formed and develop into turbulence in the next snapshot at $t^* = 4990$. Due to the rapid rotation all $\beta \neq 0$ modes are strongly damped and the turbulence will rapidly decay. It is interesting to note that for $t^* = 5072$ very little remains of the initial $(1, 0)$ mode. The last figure, at $t^* = 7118$, shows the flow after a long time when it has been laminarized and the $(1, 0)$ mode is re-formed just before the third breakdown. With the present colour scale nothing can be seen in between the last two snapshots.

The first appearance of three-dimensional structures at $t^* = 4909$ is clearly seen in figure 15 from the wall-normal and spanwise components of the fluctuations. The typical pattern of oblique waves for secondary instabilities of plane waves is seen.

All three-dimensional structures are linearly stable in this case, but the formation of these structures may be enabled by the extreme amplitude of the $\alpha = 1$ mode. This process is visualized in figure 16, which shows the modal energy content at $y/\delta = 0.72$ for the same times as for the snapshots in figure 14. Initially, for $t^* = 4827$,

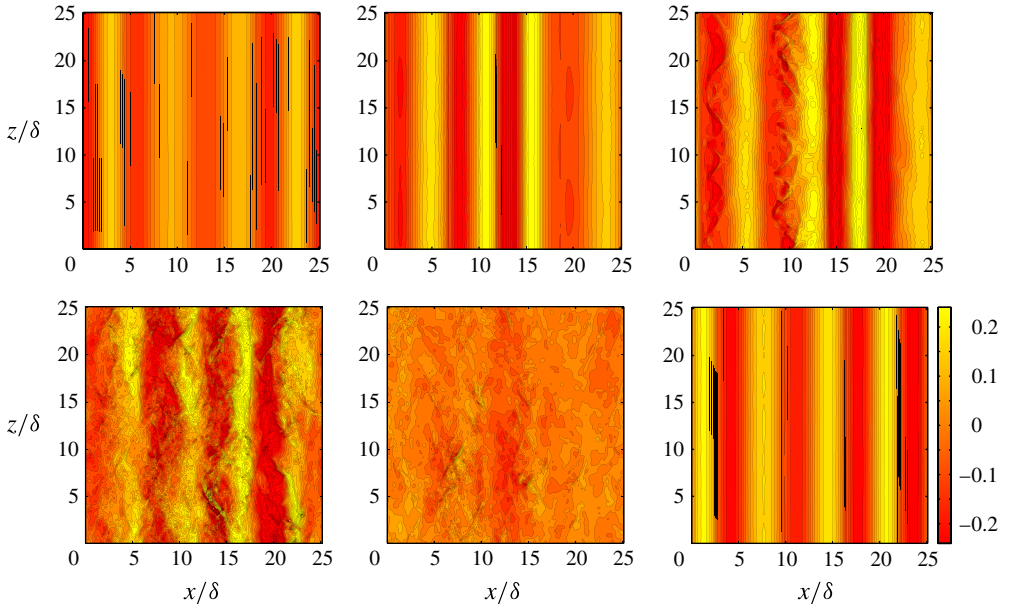

FIGURE 14. Snapshots of streamwise velocity fluctuations, u/U_b^{lam}, at $y/\delta = 0.72$ for $t^* = tU_b^{lam}/\delta = 4827$, 4876, 4909, 4990, 5072 and 7118. The different times are marked in figure 13. Same colour scale is valid in all plots.

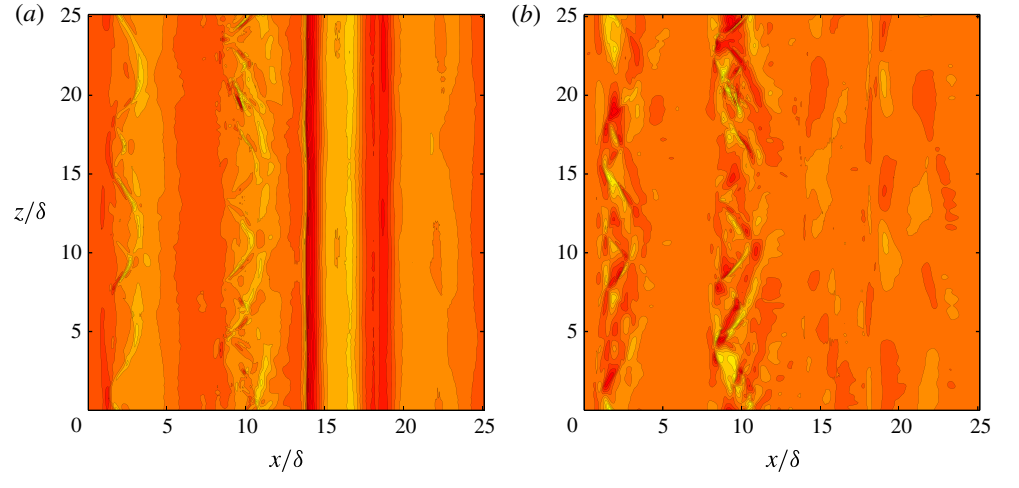

FIGURE 15. Snapshots of (*a*) wall-normal, v/U_b^{lam}, and (*b*) spanwise, w/U_b^{lam}, velocity fluctuations at $y/\delta = 0.72$ for $t^* = tU_b^{lam}/\delta = 4909$. Same colour scale as in figure 14.

we can only see the different $\beta = 0$ modes where $\alpha = 1$ dominates. There is also a small content in the (0.5, 0.25) and (1.0, 0.5) modes, which simply are residues of the previous breakdown, see figure 13(*b*). The particular position $y/\delta = 0.72$ is chosen as a good compromise for illustrating both the primary and secondary instabilities. The secondary instability turned out to be most clearly visualized at the stable side of the channel, and the energy content at $y/\delta = 0.72$ also reasonably well represents the integrated energy of the instabilities.

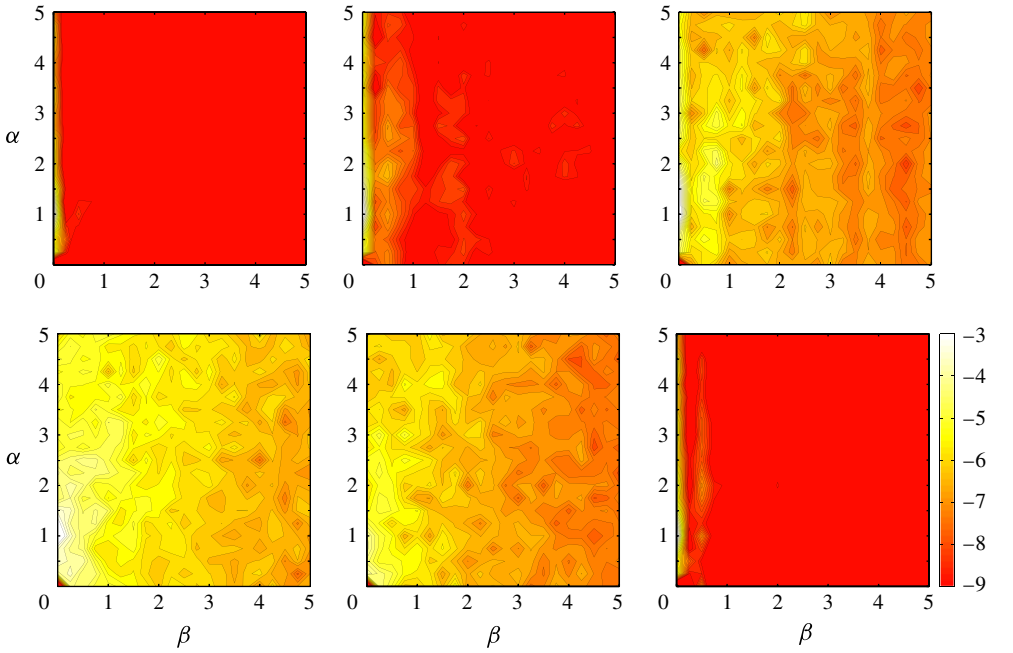

FIGURE 16. Contour plots of total energy $(\log(E(\alpha, \beta)/(U_b^{lam})^2)$ in the Fourier (α, β)-plane at the same wall-normal position and time steps as in figure 14. The mean flow $(0, 0)$ is excluded.

In the next plot in figure 16 for $t^* = 4876$ the amplitude of the $(1, 0)$ mode enables the growth of three-dimensional modes and we can see a series of different $\beta = 0.5$ modes. The third plot in figure 16 for $t^* = 4909$ shows that the turbulence energy cascade to higher wavenumbers has started. However, the energy spectrum is still dominated by the $\beta = 0$ modes, but different $\beta = 0.5$ modes have grown significantly. However, in the next plot at $t^* = 4990$ the $\beta = 0$ modes also start to break down and cascade into higher modes.

Turning our attention to figure 13(*b*) we see that the initial breakdown of the $(1, 0)$ mode consists of three stages. (i) First, the set of $\beta = 0.5$ modes (green curves) are the most rapidly growing three-dimensional modes initially up to $t^* = 4909$ while the $\beta = 0$ modes are still growing. (ii) In the next stage up to $t^* = 4990$, the $\beta = 0.25$ modes are taking over. The differences in $\beta = 0$ and $\beta = 0.5$ modes are now reduced indicating energy transfer between these modes. However, the total disturbance energy is still increasing. (iii) The third stage is a massive breakdown of all modes into turbulence, which then decays rapidly. However, some of the energy goes in the opposite direction into the $(0.25, 0)$ mode, which is the most energetic mode at this final stage at $t^* = 5072$.

6.2. *Computational box size*

The $\beta = 0.5$ modes play a key role in the breakdown of the $\beta = 0$ modes into three-dimensional structures and eventually turbulence. By reducing the computational box size to $2\pi\delta$ in the spanwise direction the $\beta = 0.5$ mode cannot be captured in the computation. The consequence is that the three-dimensional breakdown is disabled and the solution will saturate at the extreme-amplitude state, which becomes statistically steady.

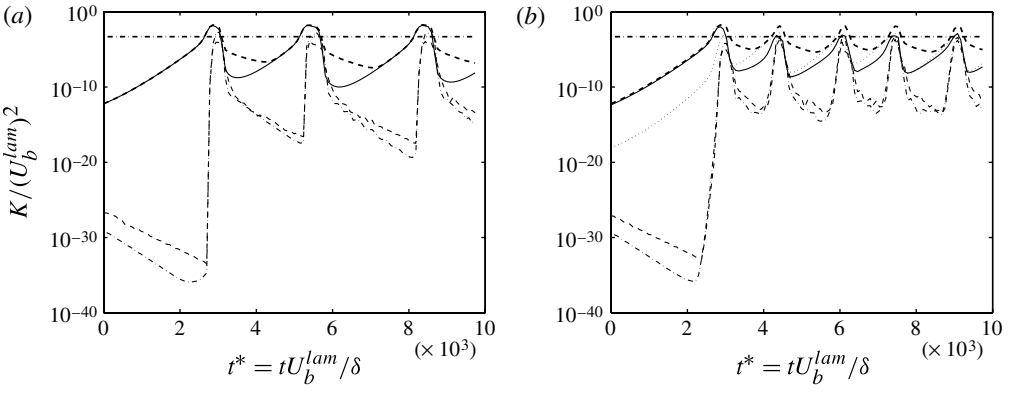

FIGURE 17. Energy for various modes integrated in the y-direction for the box sizes (*a*) $4\pi\delta \times 2\delta \times 4\pi\delta$ and (*b*) $16\pi\delta \times 2\delta \times 16\pi\delta$. Thick curves: total fluctuation energy K for the present case (- - -) and corresponding non-rotating turbulent case (-·-). Thin curves: $\beta = 0$ modes with $\alpha = 1.0$ (—), 0.5 (- - -) and 1.5 (-·-). Also $\alpha = 0.875$ (· · ·) is added to (*b*).

With a box size of $4\pi\delta \times 2\delta \times 4\pi\delta$, see figure 17(*a*), the $\beta = 0.5$ modes are captured but not the $\beta = 0.25$ modes. The degree of freedom for energy transfer is hence reduced, leading to an increased period. By increasing the box size to $16\pi\delta \times 2\delta \times 16\pi\delta$, see figure 17(*b*), essentially the same behaviour as for the $8\pi\delta \times 2\delta \times 8\pi\delta$ box is seen but with a somewhat decreased period. The $8\pi\delta \times 2\delta \times 8\pi\delta$ box is hence believed to be able to capture the essential dynamics of the flow. Some additional combinations of streamwise and spanwise box sizes and resolution were tested, see table 1, with essentially the same cyclic behaviour as long as the spanwise box size is at least $4\pi\delta$.

6.3. *Extreme-amplitude state*

The $(1, 0)$ mode will grow exponentially to extreme amplitudes much larger than in fully developed turbulence. The amplitude is far into the nonlinear regime which will strongly influence the mean velocity.

In figure 18, the flow is averaged in the homogeneous directions at $t^* = 4827$ just before the three-dimensional breakdown for extracting the Reynolds-averaged statistics in terms of mean velocity and fluctuation correlations. The mean velocity profile is rather close to that for laminar flow. This indicates that although the amplitude is much higher than for turbulent flows, the contribution to the mixing is much weaker than in turbulent flows.

Among the normal Reynolds stresses, the streamwise and wall-normal components dominate over the spanwise component. Compared to non-rotating turbulent channel flow, the magnitude of $\overline{uu}^+$ and $\overline{vv}^+$ is higher by at least an order of magnitude. On the other hand, the $\overline{uv}^+$ correlation is governed by the momentum equation and essentially limited to the interval ± 1.

Even though the amplitude is extremely large, the shapes of the $\overline{uu}$ and $\overline{vv}$ profiles resemble that of the TS eigenmodes with near-wall peaks for $\overline{uu}$ and a peak in the channel centre for $\overline{vv}$. The similarity with linear TS modes is striking. Also the TS modes have a very weak $\overline{uv}$ correlation, which is related to the amplification rate, typically of the order of 0.01, see figure 5. The finite-amplitude growth rate observed for the $\alpha = 1$ mode is roughly that given by the linear growth rate.

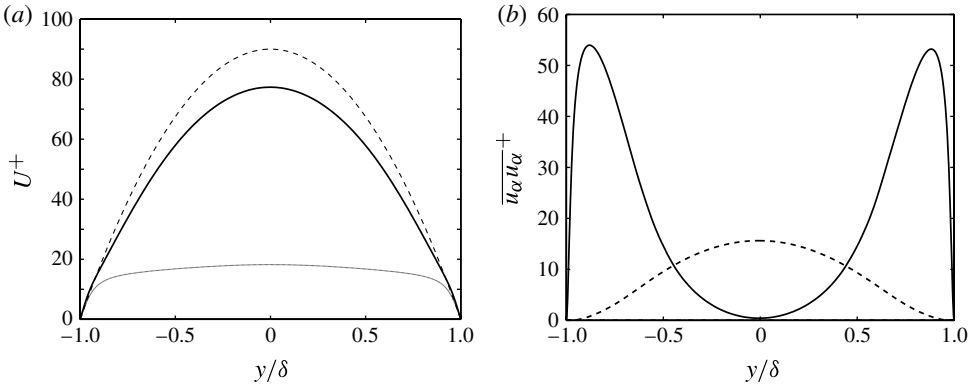

FIGURE 18. (*a*) Mean velocity in wall units (—) compared with the parabolic laminar profile (- - -) and non-rotating turbulent channel flow (-··-). (*b*) Reynolds stresses in wall units: $\overline{uu}^+$ (—), $\overline{vv}^+$ (- - -), $\overline{ww}^+$ (· · ·). $t^* = 4827$.

As a reflection of the amplitudes present here we may note that the peak-to-peak u-amplitude of the $\alpha = 1$ mode corresponds to $\sim$50 % of U_b before breakdown, signifying the fact that we here consider a saturated nonlinear state of extreme amplitude.

7. Concluding remarks

We have observed that spanwise rotating channel flow reaches a nonlinear periodic state for supercritical rotation rates with cyclic growth of disturbances, turbulence breakdown and relaminarization. The periodic flow is remarkable for several reasons. First, the fluctuations reach extreme amplitudes before breakdown. Peak r.m.s. of velocity fluctuations reach values up to 20 % of the bulk velocity. Such extremely large-amplitude fluctuations, much higher than that of typical turbulence, are rarely seen. The peak amplitude before turbulence breakdown is much higher than in other nonlinear non-turbulent states, such as for Görtler, Taylor or Dean vortices, in flows with Coriolis forces or in flows with buoyancy or Lorentz forces. Secondly, the period is extremely long, in the order of 1000 time units normalized by the channel half-height and bulk velocity. Such a time scale is more than sufficient for obtaining a statistically steady state for the non-rotating channel, and also for collecting the steady-state statistics.

The periodic state can only exist when all cross-flow modes with $\beta \neq 0$ are damped (through linear mechanisms) by the rotation. This occurs when the rotation number is larger than the critical value, Ro_c. In the absence of three-dimensional structures, two-dimensional TS modes can grow if the Reynolds number is supercritical. The TS modes will not break down to turbulence in the usual way because of the strong stabilization of three-dimensional modes needed for the turbulence cascade. Hence, the TS modes may grow to extremely high amplitudes before the nonlinearity of the TS modes will override the stabilization by rotation. Secondary instability preceding turbulence breakdown is dominated by transfer of energy to a series of $\beta \approx 0.5$ modes. Actually, it was found that these β modes are necessary for the turbulent breakdown to occur. Disabling the $\beta = 1/2$ modes by choosing a smaller $2\pi\delta$ computational box in the spanwise direction was shown to prevent breakdown to turbulence and the flow then saturates at the state of extreme-amplitude TS waves where the growth is

balanced by viscous dissipative mechanisms. The sensitivity of low β wavenumbers was found to be strong; although the turbulence breakdown was found to be captured with a $4\pi\delta \times 4\pi\delta$ box, the period for the cyclic behaviour was significantly larger than for the larger ($8\pi\delta \times 8\pi\delta$ and $16\pi\delta \times 16\pi\delta$) boxes. Hence most of the results presented were obtained with the $8\pi\delta \times 8\pi\delta$ box, which was judged to be large enough to capture all essential features of the cyclic growth and breakdown of the flow.

Some aspects of this saturated state were previously observed and documented by Lamballais *et al.* (1996), but they did not observe any turbulent breakdown in their simulation of the most rapidly rotating flow. However, the rotation rate was higher than in the present study but they also used a rather small $4\pi\delta \times 4\pi\delta$ computational box. Whether the turbulence breakdown in their simulation is prohibited by the stronger rotation rate or too small a computational box is not known.

Subcritical rotation rates result in statistically steady turbulent flow with a well-known asymmetric velocity profile with a linear region which is linearly neutrally stable. The turbulence is reduced by increasing rotation and will be completely damped at the critical rotation number, Ro_c. There is no hysteresis on increasing or decreasing Ro around Ro_c which here was shown to be very precisely determined by linear stability. Hence, linear mechanisms not only govern the transition to turbulence, but, more surprisingly, the critical rotation number also specifies when the flow will relaminarize from a fully turbulent state. The linear mechanisms are, thus, not only strongly unstable for subcritical rotation numbers but also strongly stabilized for supercritical Ro where no turbulence can be sustained. This is remarkable since in most cases neutral stability only defines when disturbances can start to grow and usually the existence of turbulence is not very strongly related to the linear stability. The linear growth rate can be extremely high, of order unity, for rotation rates slightly lower than the critical one, which is an explanation for the extremely good comparison between the theoretically and numerically determined critical rotation numbers.

Linear mechanisms have multiple roles in strongly rotating channel flows. For lower $Ro < Ro_c$ the linear part of the asymmetric turbulent velocity profile is governed by linear stability. Moreover, linearly unstable modes are superimposed on the turbulent velocity field, being more dominating as Ro_c is approached. The laminarization of the flow at $Ro = Ro_c$ is related to the fact that all cross-flow modes become linearly stable, which enables the linear, and eventually nonlinear, growth of TS waves to extreme nonlinear amplitudes with remarkably close resemblance to the linear TS eigenmode.

Acknowledgements

The present study was partly funded by the Swedish Research Council (grants no. 2008-7310 and 2010-6965). The simulations were performed on resources provided by the Swedish National Infrastructure for Computing (SNIC) at PDC Center for High Performance Computing, Royal Institute of Technology (KTH) and at National Supercomputer Centre (NSC) in Linköping. The authors would like to thank in particular one of the reviewers for comprehensive review and constructive critique that led to significant additions to the paper.

REFERENCES

ALFREDSSON, P. H. & PERSSON, H. 1989 Instabilities in channel flow with system rotation. *J. Fluid Mech.* **202**, 543–557.

BAGHERI, S. & HANIFI, A. 2007 The stabilizing effect of streaks on Tollmien–Schlichting and oblique waves: a parametric study. *Phys. Fluids* **19**, 078103.

BARDINA, J., FERZIGER, J. H. & REYNOLDS, W. C. 1983 Improved turbulence models based on large-eddy simulation of homogeneous incompressible turbulent flows. *Stanford University Tech. Rep.* TF-19.

BECH, K. H. & ANDERSSON, H. I. 1997 Turbulent plane Couette flow subject to strong system rotation. *J. Fluid Mech.* **347**, 289–314.

BRADSHAW, P. 1969 The analogy between streamline curvature and buoyancy in turbulent shear flow. *J. Fluid Mech.* **36**, 177–191.

BRETHOUWER, G. 2005 The effect of rotation on rapidly sheared homogeneous turbulence and passive scalar transport. Linear theory and direct numerical simulation. *J. Fluid Mech.* **542**, 305–342.

BRETHOUWER, G., DUGUET, Y. & SCHLATTER, P. 2012 Turbulent-laminar coexistence in wall flows with Coriolis, buoyancy or Lorentz forces. *J. Fluid Mech.* **704**, 137–172.

BRETHOUWER, G., SCHLATTER, P. & JOHANSSON, A. V. 2011 Turbulence, instabilities and passive scalars in rotating channel flow. *J. Phys.: Conf. Ser.* **318**, 032025.

FRANSSON, J. H. M., BRANDT, L., TALAMELLI, A. & COSSU, C. 2005 Experimental study of the stabilization of Tollmien–Schlichting waves by finite amplitude streaks. *Phys. Fluids* **17**, 054110.

GRUNDESTAM, O., WALLIN, S. & JOHANSSON, A. V. 2008 Direct numerical simulations of rotating turbulent channel flow. *J. Fluid Mech.* 177–199.

HAMBA, F. 2006 The mechanism of zero mean absolute vorticity state in rotating channel flow. *Phys. Fluids* **18**, 125104.

HENNINGSON, D. S., LUNDBLADH, A. & JOHANSSON, A. V. 1993 A mechanism for bypass transition from localized disturbances in wall-bounded shear flows. *J. Fluid Mech.* **250**, 169–207.

JIMENEZ, J. 1990 Transition to turbulence in two-dimensional Poiseuille flow. *J. Fluid Mech.* **218**, 265–297.

JOHNSTON, J. P., HALLEEN, R. M. & LEZIUS, D. K. 1972 Effects of spanwise system rotation on the structure of two-dimensional fully developed turbulent channel flow. *J. Fluid Mech.* **56**, 533–559.

KRASNOV, D., ROSSI, M., ZIKANOV, O. & BOECK, T. 2008 Optimal growth and transition to turbulence in channel flow with spanwise magnetic field. *J. Fluid Mech.* **596**, 73–101.

KRISTOFFERSEN, R. & ANDERSSON, H. I. 1993 Direct simulations of low-Reynolds number turbulent flow in a rotating channel. *J. Fluid Mech.* **256**, 163–197.

LAKIN, W. D., NG, B. S. & REID, W. H. 1978 Approximations to the eigenvalue relation for the Orr–Sommerfeld problem. *Phil. Trans. R. Soc. Lond.* A **289**, 347.

LAMBALLAIS, E., LESIEUR, M. & MÉTAIS, O. 1996 Effects of spanwise rotation on the vorticity stretching in transitional and turbulent channel flow. *Intl. J. Heat Fluid Flow* **17**, 324–332.

LEZIUS, D. K. & JOHNSTON, J. P. 1976 Roll-cell instabilities in rotating laminar and turbulent channel flows. *J. Fluid Mech.* **77**, 153–175.

LIN, C. C. 1955 *The Theory of Hydrodynamic Stability*. Cambridge University Press.

LUNDBLAD, A., HENNINGSON, D. S. & JOHANSSON, A. V. 1992 An efficient spectral integration method for the solution of the Navier–Stokes equations. *Tech. Rep. FOI, FFA, SE-16490, Stockholm, Sweden*, 1992-28.

NAGATA, M. 1998 Tertiary solutions and their stability in rotating plane Couette flow. *J. Fluid Mech.* **358**, 357–378.

NAKABASHI, K. & KITOH, O. 1996 Low Reynolds number fully developed two-dimensional turbulent channel flow with system rotation. *J. Fluid Mech.* **315**, 1–29.

ORSZAG, S. A. 1971 Accurate solution of the Orr–Sommerfeld stability equation. *J. Fluid Mech.* **50**, 659–703.

SALHI, A. & CAMBON, C. 1997 An analysis of rotating shear flow using linear theory and dns and les results. *J. Fluid Mech.* **347**, 171–195.

TANAKA, M., KIDA, S., YANASE, S. & KAWAHARA, G. 2000 Zero-absolute-vorticity state in a rotating turbulent shear flow. *Phys. Fluids* **12** (8), 1979–1985.

TSUKAHARA, T., TILLMARK, N. & ALFREDSSON, P. H. 2010 Flow regimes in a plane Couette flow with system rotation. *J. Fluid Mech.* **648**, 5–33.

WALL, D. P. & NAGATA, M. 2006 Nonlinear secondary flow through a rotating channel. *J. Fluid Mech.* **564**, 25–55.

WEIDEMAN, J. A. C & REDDY, S. C. 2000 A MATLAB differentiation matrix suite. *ACM Trans. Math. Softw.* **26** (4), 465–519.

WU, H. & KASAGI, N. 2004 Effects of arbitrary directional system rotation on turbulent channel flow. *Phys. Fluids* **16** (4), 979–990.

YANASE, S., TANAKA, M., KIDA, S. & KAWAHARA, G. 2004 Generation and sustenance mechanisms of coherent vortical structures in rotating shear turbulence of zero-mean-absolute vorticity. *Fluid Dyn. Res.* **35**, 237–254.